Journal of Porous Materials (2024) 31:267–279
https://doi.org/10.1007/s10934-023-01513-4

The controlled microfluidic formation of stable mixed phase HCP/FCC-UiO-67(Zr)-benzoic acid through modification of water concentration

Tom Bailey[1] · Lina Yang[1] · Eleanor Humphreys[1] · Faye Esat[1] · Ben Douglas[1] · Nicole Hondow[1]

Published online: 16 September 2023

Abstract
This work reports the synthesis of a mixed crystal phase mesoporous metal–organic framework (MOF) through a new synthesis route. The Hexagonal Centred Planar/Face Centred Cubic mixed phase UiO-67(Zr) product was microfluidically synthesised using benzoic acid as the acid modulator. This phase ratio can be altered through changing the concentration of water present in the reaction solution. This product shows increased mesoporosity and uptake of N_2 at 77 K and 1 bar of 1083 cm^3/g, as compared to 615 cm^3/g for the product made via the traditional batch approach. This leads to an increase working capacity due to the change in isotherm type, from type I to type IV, with the uptake occurring more gradually overall as pressure increases. An increased working capacity allows for a greater range of control for the volume of N_2 stored in/released from the material. This product has only been successful in microfluidic conditions, highlighting the potential importance of this method for future synthesis of this MOF.

Keywords Metal-Organic frameworks · Microfluidics · Microporous · Mesoporous · Crystal phase

1 Introduction

Metal–Organic Frameworks (MOFs) are crystalline porous materials composed of metal containing nodes, secondary building units (SBUs), joined together by organic linker units. Universitetet i Oslo (UiO) MOFs have zirconium based SBUs joined together by dicarboxylic acid linkers [1]. The interest in these MOFs is due to their relatively high stabilities as compared to non-Zr(IV) carboxylate containing MOFs [2]. They have found uses in a range of applications, from gas storage[3–6] to catalysis [7–11], with the UiO series applicable for these applications through modifying the linker units used in synthesis or by altering the UiO product after synthesis [12].

MOFs have been used, alongside other porous materials, to enhance the storage of gases, through increased overall uptake or by increasing the selectivity for specific gases [13]. The large surface areas and open pores of the MOF can be filled, allowing for gas to be stored in higher volumes and at lower pressures when compared to storing in traditional bottles [13]. UiO MOFs in particular have been looked at in gas applications due to the high physical stabilities, allowing them to remain stable in harsher temperatures and pressures when storing or releasing the gas [14]. However, the key limitation to UiO MOFs in gas storage is their microporosity and low density. While they have high uptakes of gas in their structures, the working capacity, defined as the difference between the uptakes at a maximum pressure and that at the lowest controlled pressure, is narrow [15]. This occurs due to the micropores being filled at the low pressures and then not changing, which is a Type I adsorption isotherm.

To improve this, Connolly et al. formed densely packed monolithic UiO-66, which introduced larger mesopores and macropores into the structure, thereby increasing the overall pore volume of the structure [15]. These larger pores would only fill at higher pressures, allowing for a steady increase of adsorption as the pressure increased, leading to a higher working capacity. Connelly et al. therefore showed that if mesopores and macropores are introduced into the UiO structure there can be an increase the gas uptake while also raising the working capacity, and this can be achieved through modification or by introducing defects into the

✉ Tom Bailey
pmtwb@leeds.ac.uk

[1] School of Chemical and Process Engineering, University of Leeds, Leeds LS2 9JT, UK

structure. Alongside introducing larger pores, they also increased the density of the UiO-66 structure through sol gel synthesis and varying drying conditions, finding a key trend. As density increased, the level of mesoporosity decreased in the structures, leading to N_2 isotherms which followed a Type I shape and with lower overall uptakes [15]. This decrease in mesoporosity is not due to the mesopores not arising due to defects or change in structure, but due to the spacing between crystalline UiO-66 particles.

Defects may appear in UiO MOFs, either as missing linker unit or as missing cluster units, and are introduced either by design or as a by-product of using certain acid modulator groups [16]. Missing linker defects can occur when there is a "capping" group available, that will bind to the metal cluster instead of the linker unit, making the site unavailable [17]. These capping groups are usually monocarboxylic acids, such as acetic or benzoic acid, but can also other chemicals such as water. By having these groups competing/exchanging with the linker units for space on the clusters, they can have a significant impact on the reaction kinetics and the structure [1, 17]. Defects can have a large effect on the structures pore size, surface area and reactivity, so being able to control these consistently is a point of focus [18].

An engineering focus for the UiO series MOFs has been to introduce enough missing linker defects into the structure that the MOF changes from its usual face centred cubic (FCC) structure to a hexagonal centred planar (HCP) structure [19]. By increasing the number of missing linker defects present in the structure, the metal clusters join together, changing from the 12 linker coordinated $Zr_6O_4OH_4$ (FCC) to the 18 linker coordinated $Zr_{12}O_8OH_{14}$ (HCP) [20] (Fig. 1).

Success in HCP synthesis has been found by increasing the concentration of water present in the reaction to achieve the desired product, in which the water molecules will act as capping agents and promote the formation of HCP [20]. Previous HCP products have been found to perform better than their traditional FCC counterparts in certain ways, such as increased adsorption of perfluorooctanesulfonate when compared to defect free FCC UiO-66 [21], or an increase in catalytic activity for ring-opening reactions of epoxides due to a higher density of defect sites [22]. While the adsorption has increased, the surface area for the HCP products is usually less than their original FCC forms, due to the loss of linkers and clusters combining, so this increase in adsorption is attributed to some mesopores now being present in these products, allowing for higher uptakes [23]. This has been seen in previous nitrogen isotherms for these products, with a type II isotherm being present instead of type I as usually seen, with larger pores only being filled at higher pressures [20]. Distinguishing between these two structures is achieved through X-ray diffraction (XRD), with the FCC product showing (111) and (200) as key diffraction peaks, while the HCP products shows (002) and (100) diffraction peaks (Fig. 2).

Previous examples of HCP-UiO-67 have used formic acid as the modulator group, for both Hf and Zr versions [19, 25]. Being able to achieve the HCP structure while using different acid modulator groups would allow for different functional groups to be present in the structure, leading to further applications. Incorporating benzoic acid into to the structure would allow for more ring-based interaction to occur in the pores, such as π–π bonding. Work by Zhang et al. found that the adsorption of toluene on UiO-67 was increased when using benzoic acid as the modulator, due to the missing linkers increasing the pore size, but also due to the π–π interactions between the benzoic acid and the toluene [26]. Density Functional Theory calculations performed by Zhao et al. found that bonding through these π–π interactions is the most likely pathway for toluene and various other volatile solvents [27].

Another key point of interest in developing MOFs for industry use is the transfer of traditionally long and expensive batch synthesis processes to faster continuous synthesis, through the use of microfluidic reactors [28–30]. These reactors enable a higher level of reaction control by the high surface area to volume ratio of the small channels in which the reaction mixture passes through, which gives increased heat transfer, mass transfer and mixing. Previous work in our group has succeeded in forming FCC-UiO-67(Zr) in a reaction time of 30 min of heating as compared to the traditional 24 h due to this increased heat/mass transfer [31]. By exploiting the properties possible in microfluidics, it may assist in forming HCP-UiO-67(Zr)

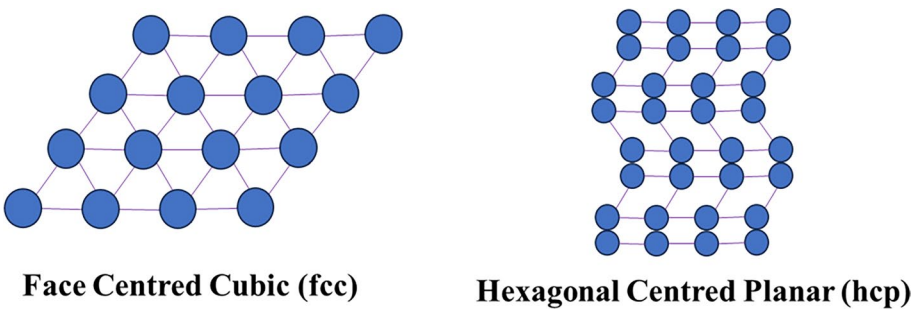

Fig. 1 General 2D representation of face centred cubic (fcc) and hexagonal centred planar (hcp) structures. Blue circles represent SBU's and purple lines represent linkers (Color figure online)

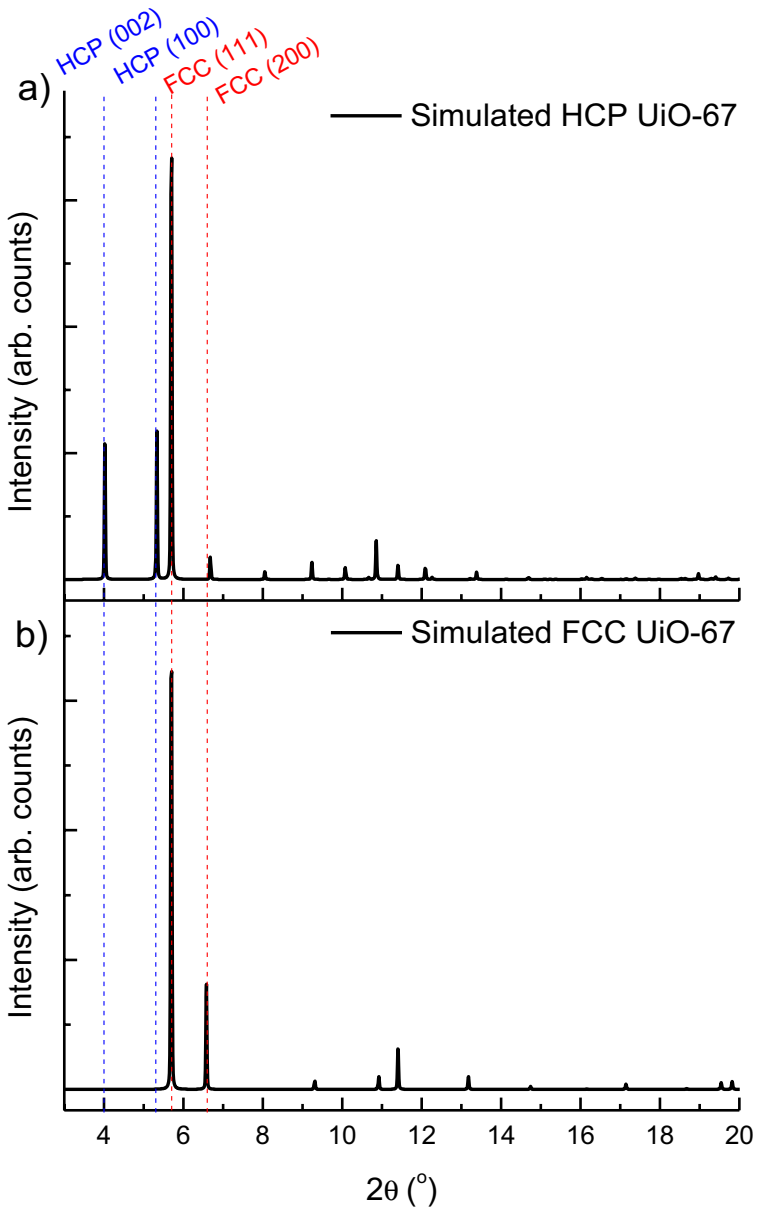

Fig. 2 Simulated XRD patterns for **a** HCP UiO-67 and **b** FCC UiO-67. Patterns were simulated in VESTA. CIF for HCP is from Cliffe et al.'s SI [19]. CIF for the FCC pattern was obtained from the Cambridge Structural Database, from a paper by Goodenough et al. [24] (Color figure online)

while using benzoic acid as the modulator species. Firstly, previous work has shown that higher temperatures increase the formation of metal-oxide clusters with higher nuclearity, with the rate for FCC formation being higher than that for HCP at lower temperature [19]. Therefore, if a reaction gives a product with a higher HCP to FCC ratio then the reaction should be quickly cooled after its heating has been performed, which is possible with microfluidics.

The aim for this work was to synthesise HCP-UiO-67(Zr) using benzoic acid as the modulator species, while varying the water content present to examine the effect this has on the resulting product. The best product found was then re-synthesised using similar conditions in batch, to see if the use of microfluidics influences the product. These products were analysed using XRD and N_2 isotherms, all with comparison to a traditionally batch synthesised FCC-UiO-67 (Zr) product. Comments on the synthesis procedure and improvements for future work are provided.

2 Materials and methods

2.1 Chemicals

Zirconium chloride (98%, Cat number: L14891) and silicon oil (Cat number: A12728.36) were purchased from Alfa Aesar. Benzoic acid (99%, Cat number: 237766) and biphenyl dicarboxylic acid (BPDC; 95%, Cat number: 091522) were purchased from Fluorochem. Methanol

(> 99.9%, Cat number: 34860-2.5L-R) and dimethylformamide (DMF; > 99.9%, Cat number: 27054) were purchased from Sigma Aldrich. DMF and methanol were dried using 3 Å molecular sieve beads, to control the water content present in the reactions, purchased from Avantor (L05359.30).

2.2 Microfluidic synthesis of UiO-67 products

The general setup for the coiled flow invertor reactor (CFIR) and majority of the synthesis procedure is provided in our previous work [31]. The CFIR had a reactor length of 4.018 m with an inner diameter of 0.79×10^{-3} m, giving a volume of 1.96 ml within the reactor. The residence time used was 30 min, leading to a flowrate of 0.0653 ml/min. This results in an overall synthesis time of ~ 2.6 h.

Briefly, $ZrCl_4$ (60 mg, 0.26 mmol), benzoic acid (160 mg, 1.13 mmol), DMF (10 ml, 128.3 mmol) and ultrapure water were placed into a beaker and sonicated for 3 min. The water was varied from 0 to 70 molar equivalents (0–350 µl), increasing every 10 equivalents (50 µl) in relation to the molar equivalents of $ZrCl_4$. Following sonication, BPDC (62.5 mg, 0.26 mmol) was added and sonicated again for 1 min. Sonication was performed to assist with dissolving the reactants but stirring was still required within the syringe throughout the run. The reactant solution was then drawn into a 20 ml syringe with a small magnet placed inside. This was then connected to the CFIR which had been filled with dried DMF and heated to 140 °C in the oil bath. A Duran bottle, for product collection, was connected to the reactor and a nitrogen cylinder, the syringe pump was started. As the reactants were pumped through, the pressure in the system was increased slowly before the reactant solution reached the oil bath (so no reaction started before the desired pressure of 2 bar absolute was reached). This slow increase in pressure was required to ensure that the pump did not stall. Once the reactant solution had been pushed through, 2 ml of dried DMF was pushed through the reactor at the same rate, to ensure any reactant/product left is removed.

As detailed in Sect. 3.4, this work takes particular care with the use of dried solvents and an increased washing time, with the product soaked in dried methanol over 4 days, with the methanol changed every 24 h through centrifuge (6000 rpm, 15 min), before drying overnight at 120 °C. The use of dried solvents and increased washing times were key to avoid issues that are shown later in this work. The product weights ranged from ~ 5 to ~ 40 mg, depending on the concentration of water used, with higher concentrations generally leading to more product.

2.3 Traditional batch synthesis of UiO-67 [Batch]

Using the procedure given by Schaate et al. [1], $ZrCl_4$ (180 mg, 0.77 mmol), BPDC (187.5 mg, 0.77 mmol), benzoic acid (480 mg, 3.93 mmol) and dried DMF (30 ml, 385 mmol) were placed in an autoclave. This was sealed and placed in an oven at 120 °C for 24 h. The autoclave was then removed and left to cool for 2 h before opening. The products were washed with fresh DMF (2 × 30 ml) and the left to soak in methanol for 48 h, changing the methanol after 24 h by centrifuge (6000 rpm, 15 min). The product was then dried overnight at 120 °C, leaving a white power (138.4 mg).

2.4 Batch synthesis: 30 min, 140 ℃, 60 equivalent water [Batch60eq]

$ZrCl_4$ (180 mg, 0.77 mmol), BPDC (187.5 mg, 0.77 mmol), benzoic acid (480 mg, 3.93 mmol), dried DMF (30 ml, 385 mmol) and ultrapure water (900 µl, 46 mmol) were placed in an autoclave. This was sealed and placed in an oven at 140 ℃ for 30 min. The autoclave was then removed and left to cool for 2 h before opening. The products were washed with fresh DMF (2 × 30 ml) and the left to soak in methanol for 96 h, changing the methanol every 24 h by centrifuge (6000 rpm, 15 min). The product was then dried overnight at 120 °C, leaving white needles (109.3 mg).

2.5 Characterisation

XRD was performed on each of the samples formed, using a Bruker D8 with copper k-alpha source (λ = 1.5406 Å). Scan conditions were 2Theta = 3°–18° at 0.5°/min, which is equivalent to a step-size of 0.01649°. Baselines were removed in Highscore using Sonneveld and Visser baseline reduction, with granularity = 15, a bending factor of 0. The data was then automatically smoothed using Fast Fourier smoothing with a degree of smoothing = 5. Before XRD, the samples would be dried overnight at 120 °C. Simulated XRD data were performed using Vesta, with the CIF for the HCP product being taken from the supporting information of the work by Cliffe et al. [19]. The CIF for the FCC product was obtained from the Cambridge Structural Database, from a paper by Goodenough et al. [24]. For the N_2 isotherms, the samples would first be dried in air overnight at 120 °C, which was then followed by 3 h of degassing under N_2 at 220 °C. The N_2 uptake was measured at 77 K using a liquid nitrogen bath. Each isotherm was measured up to 1 bar using a Tristar 3000. Transmission electron microscopy (TEM) was conducted on an FEI Titan^3 Themis G2 operating at 300 kV fitted with 4 EDX silicon drift detectors, multiple STEM detectors, and a Gatan One-View CCD. TEM samples

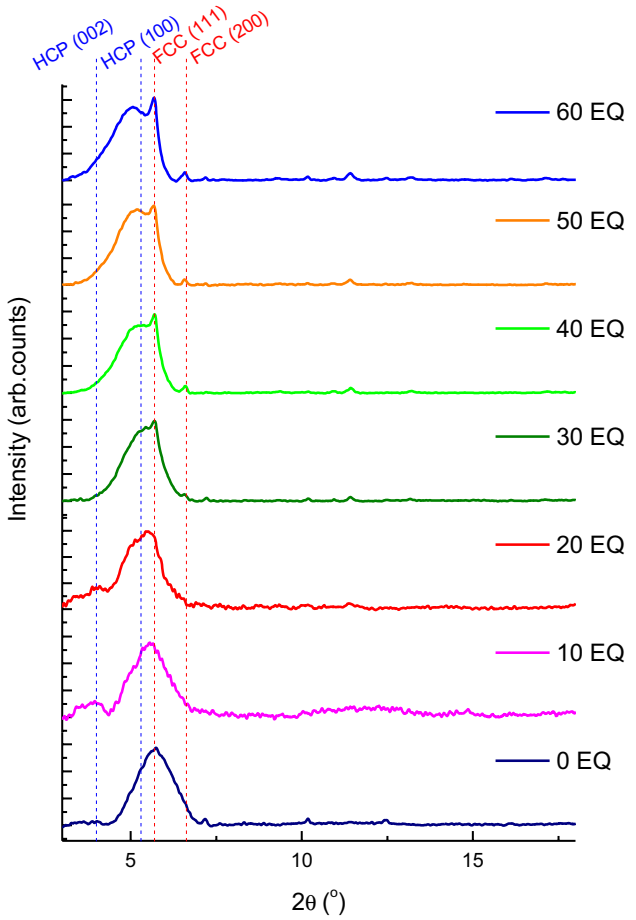

Fig. 3 XRD patterns for microfluidic UiO-67 products, with the equivalents of H_2O used varying from 0 to 60. Baseline was removed in Highscore using Sonneveld and Visser baseline reduction (Color figure online)

were prepared by dispersing the powder in methanol, with a drop placed on a continuous carbon coated copper grid.

3 Results and discussion

3.1 Structure analysis

XRD was performed on each sample, with the comparison for each shown in Fig. 3. This clearly shows that as the concentration of water present in the reactant solution increases, the HCP:FCC ratio also increases, with the peak at 5° 2θ indicative of the HCP phase growing in relative intensity. It is proposed that the (002) reflection at 4.0° 2θ and (100) at 5.3° 2θ in the HCP phase are broad and therefore overlap, causing the peak to be at 5° 2θ. This broadness and resultant overlapping of the peaks is more likely in these microfluidic products due to their smaller crystallite size (TEM for the 60 eq product is shown in Fig S1 and S2). This decrease in crystallite size was also found in previous work when forming FCC UiO-67 under the same residence time and temperature [31].

Firstly, for the 0 eq and 10 eq patterns, a single broad peak appears for them at ~ 5.7° 2θ, which is the (111) reflection for the FCC form. This is to be expected, with uncrystalline FCC-UiO-67 being formed due to the low reaction rate and to lack of defects introduced to form HCP-UiO-67. For the 20 eq sample, a new peak starts to appear at lower angles on the initial broad peak, indicating the presence of HCP-UiO-67. The centre of the single XRD peak is shifted to a lower angle, due to the increased formation of HCP phase. For the samples with higher concentrations of water (30 – 60 molar equivalents), that show two key peaks, 5.0° 2θ (combination of (002) and (100) HCP reflections) and 5.7° 2θ ((111) FCC reflection), the position of the overlapping HCP peak continues towards lower angles as the concentration of H_2O increases, while the position of the FCC peak stays the same. This demonstrates that the ratio of HCP:FCC is increasing, with the peak shifting towards the lower angles as the concentration of the (002) and (100) reflections increase in relation to the (111) reflection in the FCC. The central position for the combined HCP 002 and HCP 100 and the central position for the FCC (111) peak, in relation to the equivalents of water used in the synthesis Fig. 4.

This shift in HCP peak position is due to a secondary effect of the added water to the reaction. The products become more crystalline with increase in water, as this increases the rate formation for Zr MOFs, by "favouring hydrolysis of the zirconium precursor" [32]. This leads to those samples with higher concentrations of H_2O showing peaks at ~ 5.0° 2θ and 5.7° 2θ as separate peaks as opposed to one [32]. The 60 equivalent product shows the highest level of crystallinity and ratio of HCP:FCC, with the ratio of relative peak intensities (when comparing the HCP 5° 2θ and FCC 5.7° 2θ peaks) being almost 1:1, alongside the decreasing HCP peak position and constant FCC position as shown in Fig. 3. A higher concentration of water (70 equivalents) was attempted; however, resulting issues with its synthesis are discussed in a later Sect. 3.4.

With the 60 equivalent sample being found to contain the highest mixed phase ratio (through the shifting peak positions and peak intensity), the synthesis was repeated using a batch method, to determine the effect of the microfluidic synthesis. As can be seen in Fig. 5, the batch method formed purely FCC product. While the autoclave used for heating the reaction mixture was cooling (~ 2 h to ensure it could be opened safely), the synthesis reactions continued and as discussed earlier, the FCC phase synthesis has a higher reaction rate at lower temperatures [19]. The FCC product formed in this cooling stage will be highly crystalline, leading to a completely FCC XRD pattern (due to the high relative

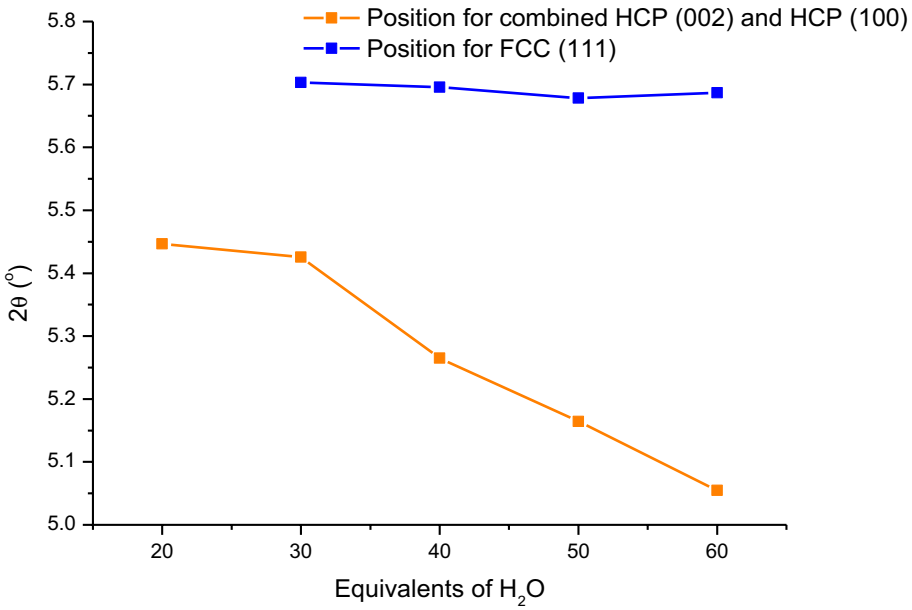

Fig. 4 HCP and FCC peak positions for microfluidically formed UiO-67, from 20 to 60 equivalents of water. 20 EQ sample only shows one clear peak, so the centre of this is listed as the HCP peak (Color figure online)

intensities of these peaks). From now on, for ease of reading, the traditional batch UiO-67(Zr) shall be referred to as **Batch**, the batch product formed using the similar reaction conditions as the 60 equivalent H_2O microfluidic product shall be referred to as **Batch60eq** and the 60 equivalent H_2O microfluidic UiO-67(Zr) product shall be referred to as **MF60eq**.

Figure 6 shows the XRD pattern for MF60eq in more detail, with sections corresponding to each reflection present highlighted. The highlighted sections of the peaks show the contribution of the FCC and HCP phases, with the MF60EQ product clearly being made up of two phases due to the peaks at both 6.63° 2θ and 7.1° 2θ, with the peak at 7.1° 2θ corresponding to the (102) diffraction peak present in the HCP phase. The presence of the hexagonal nanosheet phase found in the work by Cliffe et al. was considered due to the presence of a peak at 7.2° 2θ in the theoretical pattern for this product [19]. However, it was discounted as two much larger peaks at 5.34° 2θ and 6.47° 2θ should also be present in the pattern and since they are not it can be concluded that the peak at 7.2° 2θ in this pattern is not due to hexagonal nanosheet phase.

The diffraction peak at 7.2° 2θ is also observed in the Fast Fourier Transform (FFT) taken from TEM images of the **MF60EQ** product (Fig. S1).

It may be possible to achieve the same product formed by the microfluidic reactor in a batch synthesis by applying quenching to the reaction vessel to speed up the rate of cooling; however, this would also incur costs and potential hazards.

3.2 Gas uptake

For each of the microfluidic products formed, N_2 isotherms were performed to determine how surface area, pore volume and overall gas uptake varied with water content. Figure 7 shows the maximum N_2 uptake for each product produced through the flow synthesis at 1 bar and 77 k.

As shown, the uptake of N_2 steadily increases to 50 equivalents of water with a sudden increase in the overall uptake after this point. This corresponds with the ratio of HCP:FCC increasing in the product, with **MF60eq** showing an N_2 uptake of 1083 cm^3/g. Isotherms were also performed on **Batch** and **Batch60eq** for comparison, with key values present in Table 1. The uptake of the **MF60eq** surpasses the uptake for **Batch** which had an overall uptake of 615 cm^3/g. As the HCP:FCC ratio increases, the number of missing linkers present in the structure will increase [20], resulting in a higher frequency of mesopores forming, which correlates with an increasing N_2 uptake. This increase in mesopores/defects is reflected in the N_2 adsorption isotherms, with an increasing level of hysteresis as the equivalents of H_2O used increases, shown in the supporting information. Alongside this, as mentioned earlier, the water will increase the reaction rate to give a more crystalline product [17], with the resulting increased surface area and pore volume increasing the N_2 uptake. The adsorption isotherms for **Batch**, **Batch60eq** and **MF60eq** are in Fig. 8. Each microfluidic isotherm shows the same type IV isotherm while **Batch60eq** shows a mostly type I isotherm, similar to **Batch**.

A type IV isotherm suggests that **MF60eq** has mesopores present in the structure which will fill at higher pressures, whilst at lower pressures the micropores present will be filled. This isotherm type allows for a greater working

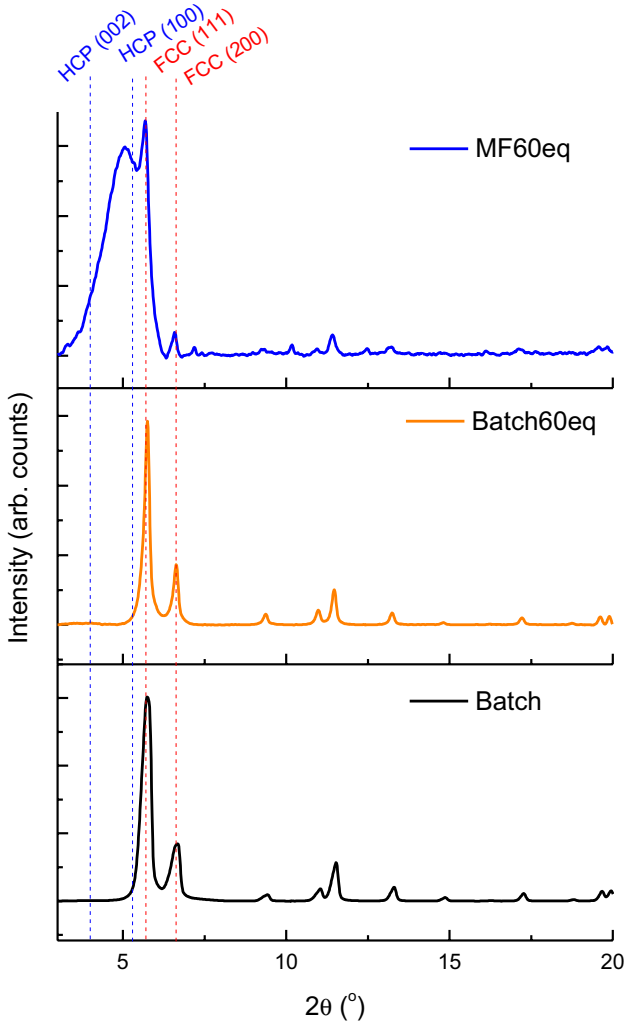

Fig. 5 XRD patterns for microfluidically synthesised HCP-UiO-67 using 60 equivalents H_2O (**MF60eq**), UiO-67 synthesised in a batch setting using similar reaction conditions to the microfluidic reaction (**Batch60eq**; 60 equivalents H_2O, 30 min heating, 140 °C) and FCC-UiO-67 synthesised using the traditional batch method (**Batch**; 0 equivalents of water, 24 h heating, 120 °C)**.** Key diffraction peaks for the HCP are highlighted at 4.0° 2θ (002) and 5.3° 2θ (100), and for FCC phase at 5.7° 2θ (111) and 6.6° 2θ (200). Baseline was removed in Highscore using Sonneveld and Visser baseline reduction (Color figure online)

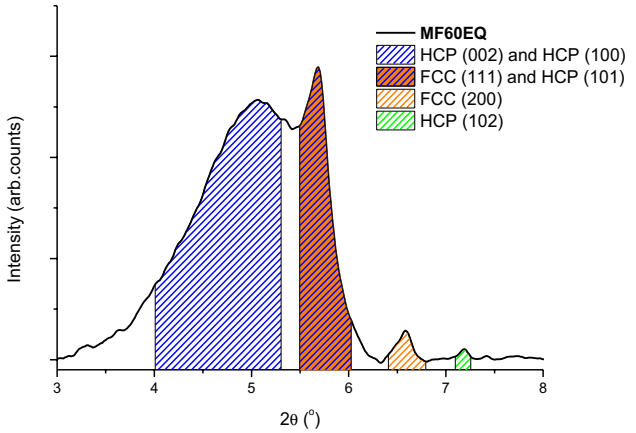

Fig. 6 XRD pattern for **MF60eq** product. Hashed lines highlight areas corresponding to different diffraction peak contributions. Baseline was removed in Highscore using Sonneveld and Visser baseline reduction (Color figure online)

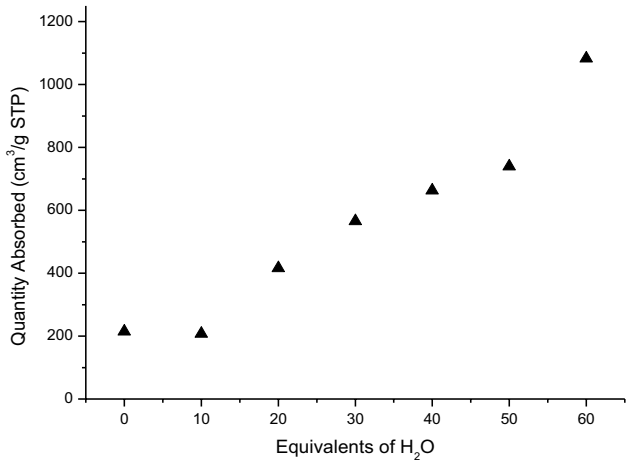

Fig. 7 Maximum quantity of N_2 adsorbed (cm^3/g) vs the molar equivalents of water used in the microfluidic reaction (Color figure online)

capacity for the material, with a larger range of uptakes available when altering the pressure, compared to **Batch** where the uptake change is negligible after the initial uptake. This isotherm shape is different to other HCP UiO products found in the literature, with two key examples to compare to. Firstly, the HCP UiO-67 product formed by Cliffe et al. showed an isotherm mostly consistent with its FCC counterpart, being mostly type I and only showing a small increase in uptake at the higher pressures [19]. This differs from what is seen here, with the majority of the uptake occurring at the higher pressure, which suggests a higher level of mesoporosity present in this structure when compared to their product. While the MOF made by Cliffe et al. is Hf based rather than Zr based, these metals are similar analogues that a direct comparison can be made [33]. Only one other example of Zr based HCP-UiO-67 has been found, in work by Dai et al. [25]. They form HCP-UiO-67 in nano-MOF form using formic acid as the modulator, achieving an uptake of ~ 1300 cm^3/g which showing a linear isotherm shape where it does not plateau, suggesting it hasn't reached its saturation pressure yet. This suggests a small level of microporosity due to the sharp initial increase in N_2 uptake, but the linear nature for the majority of the uptake suggests non-porous capture taking place, potentially surface adsorption due too the high surface area to volume ratio of nano-MOFs. While this overall uptake is closer to what is seen

Table 1 BET surface area was calculated using several points in the adsorption isotherm

	BET surface area (m^2/g)	Microporous surface area (m^2/g)	Mesoporous surface area (m^2/g)	External surface area (m^2/g)	Uptake of N_2 (cm^3/g STP)	Working capacity (cm^3/g STP)
Batch	2108 ± 29	1827 ± 85.4	43	281 ± 13	615	53
Batch60eq	1333 ± 8	380 ± 34.2	261	953 ± 86	581	237
MF60eq	837 ± 4	392 ± 20.2	232	445 ± 23	1083	870

Microporous and External areas are given by the t-plot for each isotherm, with errors provided through the errors on the t-plot intercept and slope. Mesoporous surface area is calculated using the BJH method, giving the surface area for pores with diameters between 1.7 and 300 nm. Overall uptake and working capacity are given in cm^3/g of N_2 at standard pressure and temperature (STP). Working capacity is determined by the difference in uptakes from 0.1 to 1 bar

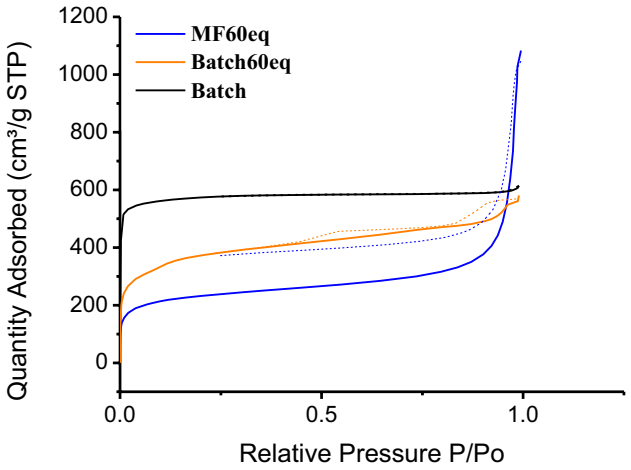

Fig. 8 N_2 isotherms for microfluidically synthesised HCP-UiO-67 using 60 equivalents H_2O (**MF60eq**), batch synthesised UiO-67 with 60 equivalents of H_2O (**Batch60eq**) and FCC-UiO-67 synthesised using the traditional batch method (**Batch**; 0 equivalents of water, 24 h heating, 120 °C). Dashed lines are for N_2 desorption (Color figure online)

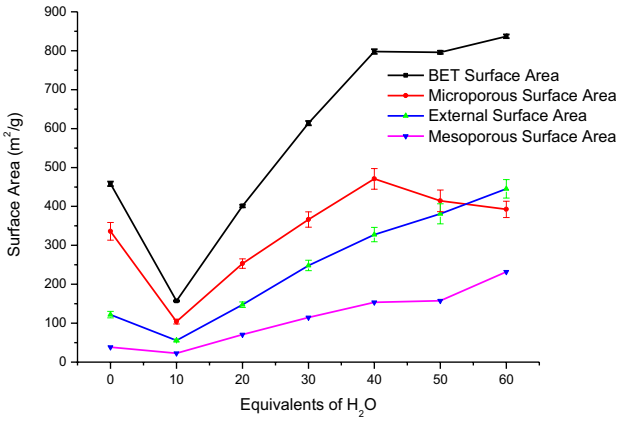

Fig. 9 Plot showing how BET, Microporous, Mesoporous and External Surface Area (m^2/g) change with the increasing concentration of water in the reaction solution. BET surface area is calculated through Brunauer, Emmett and Teller (BET) calculations, with error bars shown for these. The microporous and external areas have been calculated using t-plot calculations. The mesoporous surface area has been calculated through Barrett, Joyner, and Halenda (BJH) adsorption calculations, giving the surface area for pores with diameters between 1.7 and 300 nm. Trendlines for each data set are present to guide the eye (Color figure online)

in this work, the differing isotherm shapes suggests that the structures are different overall, with the product formed in this work being a blend of the two phases (FCC and HCP) whereas their product was purely HCP.

Figure 9 shows how the overall, microporous, mesoporous and external surface area varied across each of the microfluidic products, with the key data for **MF60eq** given in Table 1, alongside the same values for **Batch** and **Batch60eq** respectively.

Following a sharp decrease in all surface areas from the 0 equivalents H_2O product, the overall BET surface area, microporous surface area, mesoporous surface area and external surface area all increase as the water concentration increases. This is likely due to the increased reaction rate leading to more crystalline products being formed, as seen previously in the XRD (Fig. 2). At 40 equivalents of H_2O, the BET surface area stops increasing as rapidly as water concentration increases, and the microporous area starts to decrease from this point also. With increasing water concentration from 40 equivalents, the mesoporous and external surface areas continues to increase, leading

Table 2 Average pore diameter (nm), micropore volume (cm^3/g) and mesoporous volume (cm^3/g) for **Batch**, **Batch60eq**, **MF60eq**

	Average pore diameter (nm)	Micropore volume (cm^3/g)	Mesoporous volume (cm^3/g)
Batch	7.22	0.767 ± 0.005	0.079
Batch60eq	6.54	0.166 ± 0.034	0.427
MF60eq	24.52	0.167 ± 0.009	1.42

Average pore diameter and Mesoporous volume are calculated by BJH adsorption. Micropore volume is calculated through the t-plot, with errors

to the external surface area exceeding the microporous area. This correlates with the sudden increase in N_2 uptake achieved, with this higher level of mesoporosity being the key, which is reflected in the TEM for the **MF40eq**, **MF50eq** and **MF60eq** with the increased size for **hcp** particles (Figs. S1, S2, S3).

Comparing **MF60eq** to the batch products, it has a much higher overall uptake than both, despite its lower BET surface area. **Batch60eq** shows similar surface area values to the microfluidic product, with its external area exceeding its microporous area, but shows the lowest uptake of the three samples. This is due to the structural differences present in the products, which is highlighted by their pore sizes and volumes (Table 2).

While **Batch** shows a much higher micropore volume than the microfluidic product, the mesoporous volume for **MF60eq** exceeds it greatly. On the other hand, **Batch60eq** shows lower pore volumes in both categories, explaining its lower uptake even with its higher surface areas. While the pore diameters for **Batch60eq** and **Batch** products are comparable, the reduced microporous volume and increased mesoporous volume for the **Batch60eq** product suggests that it is a lower density product, with a lower number of pores per gram than in the **Batch** [34]. This may be due to the conversion of the HCP to FCC while cooling, leading to a highly defective MOF structure.

As N_2 is being adsorbed through multilayer adsorption rather than single layer adsorption, which would be found with gases that require specific binding sites to assist their uptake, the volume available to adsorb into is more important than the surface area available. Usually, as surface area increases in MOFs, so will pore volume and therefore higher uptakes of gas. However, by introducing many mesopores, the overall pore volume of **MF60eq** has managed to exceed that of **Batch**, leading to the higher uptakes.

Introducing a number of mesopores into UiO-66 has previously been done to increase the toluene adsorption ability of the material by a factor of 2.6, with the larger pores allowing for larger molecules to be more easily absorbed [35]. Alongside this, work by Zhang et al. [26], found that UiO-67 containing Benzoic acid groups and missing linker defects the uptake of toluene increased drastically, due to π- π interactions from the benzene rings on the benzoic acid and the toluene groups and the added pore volume available. From these two pieces of work, the key product formed in this work (**MF60eq**) may be highly successful at adsorbing volatile organic compounds such as toluene, with benzoic acid groups available of its surface and higher overall pore volumes than previous products.

A previous problem found with HCP UiO-66 was its lack of stability, originally degrading in ambient conditions to a hexagonal nanosheet structure after only a few days [19]. While this stability was rectified in later work [20], it is important in this work with to ensure **MF60eq** is stable. XRD was repeated on **MF60eq** after 3 and 5 months to ensure the product had not degraded (Fig. 10).

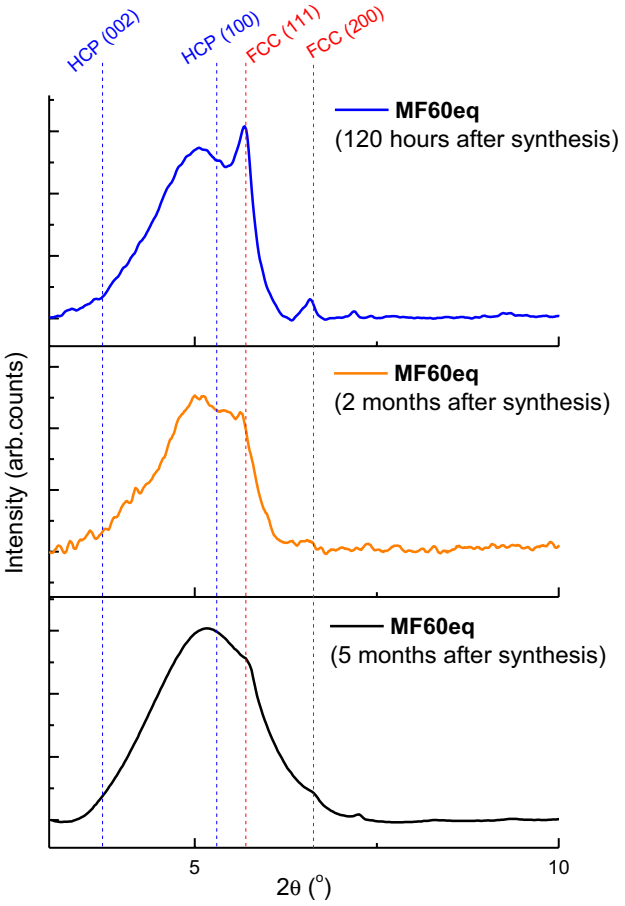

Fig. 10 XRD pattern for 3 on the day after the initial drying and 3 months after this point. Measured between 3° 2θ and 10° 2θ. Key diffraction peaks for the HCP are highlighted at 4.0° 2θ (002) and 5.3° 2θ (100), and for FCC phase at 5.7° 2θ (111) and 6.6° 2θ (200). Baseline was removed in Highscore using Sonneveld and Visser baseline reduction (Color figure online)

The degradation shown is different to what occurred in the work by Cliffe et al., with the product in their work changing from HCP to a HXL type structure, which resulted in new peaks appearing in the XRD pattern [19]. Two key factors are present in the patterns shown: Firstly, there is a loss in peak definition, which suggests that the crystal structure is amorphised overtime, indicating it may be moisture sensitive. Secondly, the position of the "HCP" peak, which was at 5.0° 2θ originally, has now shifted to a slightly higher angle for both the 3-month and 5-month products. This fits with the product becoming less crystalline, with a similar shift in the XRD to the MF products synthesised with lower equivalents of water. Rejuvenation of this product has been attempted through washing and drying but to no real success.

3.3 Difficulties present in this synthesis

There are some difficulties with the synthesis for this material that are useful for future work to be aware of. These are split into 3 distinct areas, with current or future solutions to each of these issues being given here. Firstly, as is a common issue for microfluidic work, blockages may occur in the tubing, meaning that the reactants/products currently in the reactor will need to be disposed of, as the actual residence time for these products will become unknown. This becomes a problem for this reaction at higher concentrations (70 equivalent and above) of water are used, with the increased reaction rate meaning that more product is formed earlier in the system, giving more time for a blockage to occur. A product for 70 equivalents was formed and while it showed high surface areas/uptakes (N_2 isotherm in Fig. S10), its synthesis repeatedly suffered from blockages, meaning it was not possible to keep the residence time consistent, so any product formed would be unreliable for repeat synthesis. The use of both tubing which is slightly wider (to give more space for the products/reactants to move) and a CFIR reactor with a longer pathlength (so that higher flowrates can be used for the same residence time, keeping the product from settling on the tubing) may provide future opportunity.

Secondly, similar to the problem of blockages is the issue of fouling on the tubing surface. While this leftover product may not block the flow in future reactions, it will affect any future product that passes through it. For example, Fig. 11, shows the XRD patterns for two 50 equivalent products, with one being from when the reactor was found to have had some fouling present in the tubing from a previous reaction.

The fouling product left in the tubing continued to react at room temperature, forming FCC-UiO-67 which then reacted with the new reactants through heteronuclear nucleation,

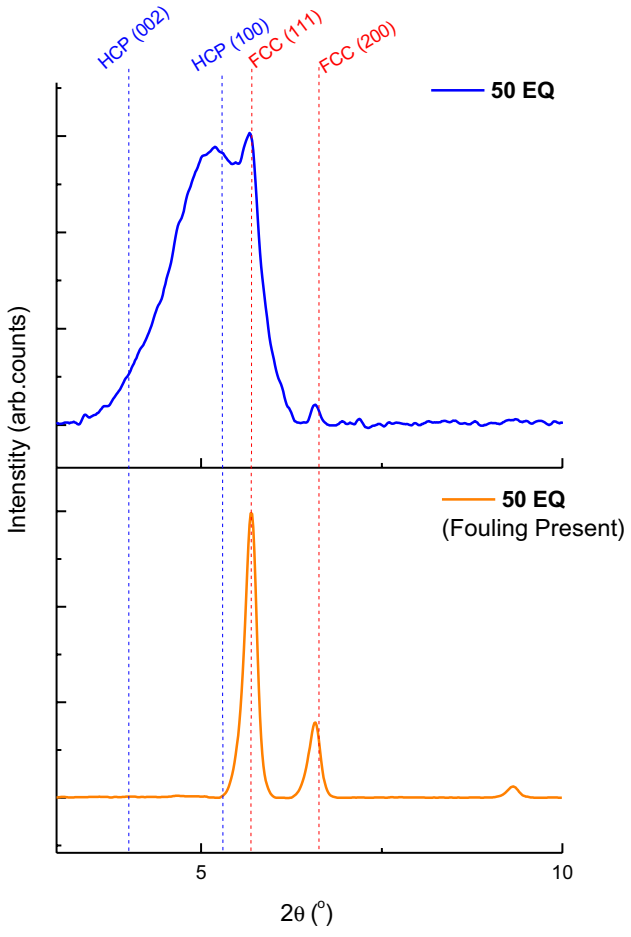

Fig. 11 XRD patterns for the 50 equivalent H_2O UiO-67 product and for the product formed under the same reaction conditions, except fouling was found to have been present in the reactor. Key diffraction peaks for the HCP are highlighted at 4.0° 2θ (002) and 5.3° 2θ (100), and for FCC phase at 5.7° 2θ (111) and 6.6° 2θ (200). Baseline was removed in Highscore using Sonneveld and Visser baseline reduction (Color figure online)

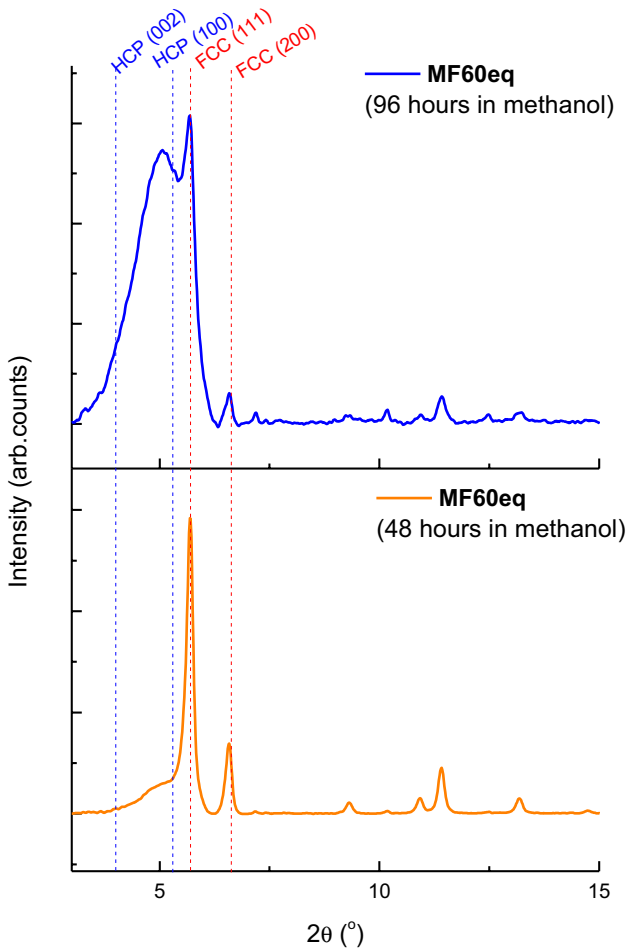

Fig. 12 XRD pattern for **MF60eq** when using 96 h washing and for **MF60eq** when using 48 h washing. Key diffraction peaks for the HCP are highlighted at 4.0° 2θ (002) and 5.3° 2θ (100), and for FCC phase at 5.7° 2θ (111) and 6.6° 2θ (200). Baseline was removed in Highscore using Sonneveld and Visser baseline reduction (Color figure online)

giving a product with a very high FCC:HCP ratio. The higher crystallinity of the FCC formed is of much higher intensity compared to the rest of the pattern.

The final challenge can be found in the drying and washing stage. Extra care has to be taken when washing this product, as when a shorter washing method (48 h soaking in methanol, rather than 96) was attempted for one of the 60 equivalent product, a pattern similar to the FCC batch products was formed (Fig. 12). If there is still DMF present in the structure and it is heated, the exchange reaction between FCC and HCP phases will continue, with the rate for FCC being faster at lower temperatures as mentioned earlier, leading to this structure [19].

The XRD pattern for the product with shorter washing does suggest that the HCP phase is still present, due to the low intensity broad peak appearing at 5° 2θ, with the HCP being lower intensity in the pattern when compared to the highly crystalline FCC. The N_2 isotherm for this product supports this theory as well, with a Type IV N_2 isotherm being present (Fig. S12).

4 Conclusions

A mixed Hexagonal Centred Planar (HCP) and Face Centred Cubic (FCC) phase UiO-67(Zr) product has been formed with benzoic acid as the acid modulating group, using microfluidics. Increasing the volume of water used in the synthesis had two key effects: increasing the synthesis rate and driving the synthesis towards the HCP phase product. Increasing the molar ratio of water to $ZrCl_4$ higher than 60:1 led to an increased level of fouling/blockages within the reactor, so future work should look to adapt the reactor for the use of higher water concentrations, tipping the product towards being purely HCP. Microfluidic synthesis was found to be vital to this process, with its increased heat transfer and rapid cooling allowing for the HCP phase synthesis to be promoted while the FCC phase was suppressed where possible, with synthesis under similar conditions in isothermal batch synthesis resulting in a different product being formed. The microfluidic produced material with 60 equivalents of water (**MF60eq**) showed a higher uptake of N_2 than that found for the traditional UiO-67 product (1083 cm^3/g compared to 615 cm^3/g), with a type IV isotherm resulting from the increased mesoporosity of the structure. This different isotherm type gives a higher working capacity for N_2, at 870 cm^3/g compared to 53 cm^3/g for the traditional batch UiO-67. Various difficulties with this synthesis have been highlighted, with future work aiming to reduce the effect of these issues and synthesise a product with a higher HCP:FCC ratio while still using benzoic acid as the modulating group.

Supplementary Information The online version contains supplementary material available at https://doi.org/10.1007/s10934-023-01513-4.

Acknowledgements Financial support from the EPSRC is gratefully acknowledged by TB in the form of studentship (EP/R513258/1; Award Number 2282152).

Author contributions Study conception and design was performed by TB and NH. Material synthesis, data collection and analysis were performed by TB and EH. Assistance in the laboratory was given by LY. FE assisted with the collection and analysis of XRD data. BD assisted in the collection and analysis of N_2 adsorption isotherms. The manuscript was written by TB and NH, with all authors commenting on and approving the manuscript.

Funding This work was funded through financial support from EPSRC Doctoral Training Partnership (EP/R513258/1).

Data availability Supplementary Information (including N_2 isotherms for all products) will be provided as a pdf document.

Code availability Not applicable.

Declarations

Conflict of interest The authors declare no competing interests.

References

1. A. Schaate, P. Roy, A. Godt, J. Lippke, F. Waltz, M. Wiebcke, P. Behrens, Modulated synthesis of Zr-based metal-organic frameworks: from nano to single crystals. Chemistry **17**, 6643–6651 (2011). https://doi.org/10.1002/chem.201003211
2. J.H. Cavka, S. Jakobsen, U. Olsbye, N. Guillou, C. Lamberti, S. Bordiga, K.P. Lillerud, A new zirconium inorganic building brick forming metal organic frameworks with exceptional stability. J. Am. Chem. Soc. **130**, 13850–13851 (2008). https://doi.org/10.1021/ja8057953
3. R. Vaidhyanathan, S.S. Iremonger, K.W. Dawson, G.K.H. Shimizu, An amine-functionalized metal organic framework for preferential CO_2 adsorption at low pressures. Chem. Commun. **35**, 5230–5232 (2009). https://doi.org/10.1039/b911481e
4. D. Han, F.L. Jiang, M.Y. Wu, L. Chen, Q.H. Chen, M.C. Hong, A Non-interpenetrated porous metal-organic framework with high gas-uptake capacity. Chem. Commun. **47**, 9861–9863 (2011). https://doi.org/10.1039/c1cc12858b
5. Z. Chen, S. Xiang, H.D. Arman, P. Li, D. Zhao, B. Chen, Significantly enhanced CO_2/CH_4 separation selectivity within a 3D prototype metal-organic framework functionalized with OH groups

on pore surfaces at room temperature. Eur. J. Inorg. Chem. **14**, 2227–2231 (2011). https://doi.org/10.1002/ejic.201100034
6. K. Sumida, C.M. Brown, Z.R. Herm, S. Chavan, S. Bordiga, J.R. Long, Hydrogen storage properties and neutron scattering studies of Mg2(Dobdc)—a metal-organic framework with Open Mg2+ adsorption sites. Chem. Commun. **47**, 1157–1159 (2011). https://doi.org/10.1039/c0cc03453c
7. J. Lee, O.K. Farha, J. Roberts, K.A. Scheidt, S.T. Nguyen, J.T. Hupp, Metal–organic framework materials as catalysts. Chem. Soc. Rev. **38**, 1450–1459 (2009)
8. C.C. Hou, T.T. Li, S. Cao, Y. Chen, W.F. Fu, Incorporation of a $[Ru(Dcbpy)(Bpy)_2]^{2+}$ photosensitizer and a $Pt(Dcbpy)Cl_2$ catalyst into metal-organic frameworks for photocatalytic hydrogen evolution from aqueous solution. J. Mater. Chem. A **3**, 10386–10394 (2015). https://doi.org/10.1039/c5ta01135c
9. A.M. Abdel-Mageed, B. Rungtaweevoranit, M. Parlinska-Wojtan, X. Pei, O.M. Yaghi, R. Jürgen Behm, highly active and stable single-atom Cu catalysts supported by a metal-organic framework. J. Am. Chem. Soc. **141**, 5201–5210 (2019). https://doi.org/10.1021/jacs.8b11386
10. M. Liu, J. Wu, H. Hou, Metal–organic framework (MOF)-based materials as heterogeneous catalysts for C−H bond activation. Chemistry **25**, 2935–2948 (2019). https://doi.org/10.1002/chem.201804149
11. C.-D. Wu, M. Zhao, Incorporation of molecular catalysts in metal–organic frameworks for highly efficient heterogeneous catalysis. Adv. Mater. (2017). https://doi.org/10.1002/adma.201605446
12. C. Kutzscher, G. Nickerl, I. Senkovska, V. Bon, S. Kaskel, Proline functionalized UiO-67 and UiO-68 type metal-organic frameworks showing reversed diastereoselectivity in aldol addition reactions. Chem. Mater. **28**, 2573–2580 (2016). https://doi.org/10.1021/acs.chemmater.5b04575
13. R.E. Morris, P.S. Wheatley, Gas storage in nanoporous materials. Angew. Chemie - Int. Ed. **47**, 4966–4981 (2008). https://doi.org/10.1002/anie.200703934
14. L. Li, S. Tang, C. Wang, X. Lv, M. Jiang, H. Wu, X. Zhao, High gas storage capacities and stepwise adsorption in a UiO type metal–organic framework incorporating lewis basic bipyridyl sites. Chem. Commun. **50**, 2304–2307 (2014). https://doi.org/10.1039/c3cc48275h
15. B.M. Connolly, M. Aragones-Anglada, J. Gandara-Loe, N.A. Danaf, D.C. Lamb, J.P. Mehta, D. Vulpe, S. Wuttke, J. Silvestre-Albero, P.Z. Moghadam, A.E.H. Wheatley, D. Fairen-Jimenez, Tuning porosity in macroscopic monolithic metal-organic frameworks for exceptional natural gas storage. Nat. Commun. **10**, 1–11 (2019). https://doi.org/10.1038/s41467-019-10185-1
16. C. Atzori, G.C. Shearer, L. Maschio, B. Civalleri, F. Bonino, C. Lamberti, S. Svelle, K.P. Lillerud, S. Bordiga, Effect of benzoic acid as a modulator in the structure of UiO-66: an experimental and computational study. J. Phys. Chem. C **121**, 9312–9324 (2017). https://doi.org/10.1021/acs.jpcc.7b00483
17. G. Kaur, S. Øien-ødegaard, A. Lazzarini, S.M. Chavan, S. Bordiga, K.P. Lillerud, U. Olsbye, Controlling the synthesis of metal–organic framework UiO-67 by tuning its kinetic driving force. Cryst. Growth Des. **19**, 4246–4251 (2019). https://doi.org/10.1021/acs.cgd.9b00916
18. G.C. Shearer, S. Chavan, S. Bordiga, S. Svelle, U. Olsbye, K.P. Lillerud, Defect engineering: tuning the porosity and composition of the metal-organic framework UiO-66 via modulated synthesis. Chem. Mater. **28**, 3749–3761 (2016). https://doi.org/10.1021/acs.chemmater.6b00602
19. M.J. Cliffe, E. Castillo-Martínez, Y. Wu, J. Lee, A.C. Forse, F.C.N. Firth, P.Z. Moghadam, D. Fairen-Jimenez, M.W. Gaultois, J.A. Hill, O.V. Magdysyuk, B. Slater, A.L. Goodwin, C.P. Grey, Metal-organic nanosheets formed via defect-mediated transformation of a hafnium metal-organic framework. J. Am. Chem. Soc. **139**, 5397–5404 (2017). https://doi.org/10.1021/jacs.7b00106
20. F.C.N. Firth, M.J. Cliffe, D. Vulpe, M. Aragones-Anglada, P.Z. Moghadam, D. Fairen-Jimenez, B. Slater, C.P. Grey, Engineering new defective phases of UiO family metal-organic frameworks with water. J. Mater. Chem. A **7**, 7459–7469 (2019). https://doi.org/10.1039/C8TA10682G
21. C.A. Clark, K.N. Heck, C.D. Powell, M.S. Wong, Highly defective UiO-66 materials for the adsorptive removal of perfluorooctanesulfonate. ACS Sustain. Chem. Eng. **7**, 6619–6628 (2019). https://doi.org/10.1021/acssuschemeng.8b05572
22. X. Chen, Y. Lyu, Z. Wang, X. Qiao, B.C. Gates, D. Yang, Tuning $Zr_{12}O_{22}$ node defects as catalytic sites in the metal-organic framework Hcp UiO-66. ACS Catal. **10**, 2906–2914 (2020). https://doi.org/10.1021/acscatal.9b04905
23. C. Ma, L. Zheng, G. Wang, J. Guo, L. Li, Q. He, Y. Chen, H. Zhang, Phase engineering of metal-organic frameworks. Aggregate **3**, 1–15 (2022). https://doi.org/10.1002/agt2.145
24. I. Goodenough, V.S.D. Devulapalli, W. Xu, M.C. Boyanich, T.Y. Luo, M. De Souza, M. Richard, N.L. Rosi, E. Borguet, Interplay between intrinsic thermal stability and expansion properties of functionalized UiO-67 metal-organic frameworks. Chem. Mater. **33**, 910–920 (2021). https://doi.org/10.1021/acs.chemmater.0c03889
25. R. Dai, F. Peng, P. Ji, K. Lu, C. Wang, J. Sun, W. Lin, Electron crystallography reveals atomic structures of metal-organic nanoplates with M12(M3-O)8(M3-OH)8(M2-OH)6 (M = Zr, Hf) secondary building units. Inorg. Chem. **56**, 8128–8134 (2017). https://doi.org/10.1021/acs.inorgchem.7b00845
26. X. Zhang, X. Shi, Q. Zhao, Y. Li, J. Wang, Y. Yang, F. Bi, J. Xu, N. Liu, Defects controlled by acid-modulators and water molecules enabled UiO-67 for exceptional toluene uptakes: an experimental and theoretical study. Chem. Eng. J. **427**, 131573 (2022). https://doi.org/10.1016/j.cej.2021.131573
27. Q. Zhao, Q. Du, Y. Yang, Z. Zhao, J. Cheng, F. Bi, X. Shi, J. Xu, X. Zhang, Effects of regulator ratio and guest molecule diffusion on VOCs adsorption by defective UiO-67: experimental and theoretical insights. Chem. Eng. J. **433**, 134510 (2022). https://doi.org/10.1016/j.cej.2022.134510
28. G. Hu, L. Yang, Y. Li, L. Wang, Continuous and scalable fabrication of stable and biocompatible MOF@SiO2 nanoparticles for drug loading. J. Mater. Chem. B **6**, 7936–7942 (2018). https://doi.org/10.1039/c8tb02308e
29. O. Kolmykov, J.M. Commenge, H. Alem, E. Girot, K. Mozet, G. Medjahdi, R. Schneider, Microfluidic reactors for the size-controlled synthesis of ZIF-8 crystals in aqueous phase. Mater. Des. **122**, 31–41 (2017). https://doi.org/10.1016/j.matdes.2017.03.002
30. M. Faustini, J. Kim, G.Y. Jeong, J.Y. Kim, H.R. Moon, W.S. Ahn, D.P. Kim, Microfluidic approach toward continuous and ultrafast synthesis of metal-organic framework crystals and hetero structures in confined microdroplets. J. Am. Chem. Soc. **135**, 14619–14626 (2013). https://doi.org/10.1021/ja4039642
31. T. Bailey, M. Pinto, N. Hondow, K.J. Wu, Continuous microfluidic synthesis of zirconium-based UiO-67 using a coiled flow invertor reactor. MethodsX **8**, 101246 (2021). https://doi.org/10.1016/j.mex.2021.101246
32. M. Taddei, J.A. Van Bokhoven, M. Ranocchiari, Influence of water in the synthesis of the zirconium-based metal-organic framework UiO-66: isolation and reactivity of [ZrCl(OH)2(DMF)2]Cl. Inorg. Chem. **59**, 7860–7868 (2020). https://doi.org/10.1021/acs.inorgchem.0c00991
33. O. Zaremba, J. Andreo, S. Wuttke, The chemistry behind room temperature synthesis of hafnium and cerium UiO-66 derivatives.

Inorg. Chem. Front. **9**, 5210–5216 (2022). https://doi.org/10.1039/d2qi01198k
34. S.E. Bambalaza, H.W. Langmi, R. Mokaya, N.M. Musyoka, J. Ren, L.E. Khotseng, Compaction of a zirconium metal-organic framework (UiO-66) for high density hydrogen storage applications. J. Mater. Chem. A **6**, 23569–23577 (2018). https://doi.org/10.1039/C8TA09227C
35. X. Zhang, Y. Yang, X. Lv, Y. Wang, N. Liu, D. Chen, L. Cui, Adsorption/desorption kinetics and breakthrough of gaseous toluene for modified microporous-mesoporous UiO-66 metal organic framework. J. Hazard. Mater. **366**, 140–150 (2019)